Nonreciprocal entanglement of ferrimagnetic magnons and nitrogen-vacancy-center ensembles by Kerr nonlinearity

Deyi Kong,[1] Jun Xu,[2] and Fei Wang[1,*]

[1] *School of Science, Hubei University of Technology, Wuhan 430068, China*

[2] *College of Physical Science and Technology, Central China Normal University, Wuhan 430079, China*

(Received 12 December 2023; revised 19 February 2024; accepted 14 March 2024; published 28 March 2024)

We propose a scheme to generate nonreciprocal entanglement between an yttrium iron garnet (YIG) sphere and two nitrogen-vacancy-center ensembles by magnon Kerr effects in a transmission-line resonator. By driving the YIG sphere appropriately, strong Kerr nonlinearities emerge and then induce magnon parametric amplification and magnon frequency shift, resulting in the appearance of optimal entanglements. Depending on the direction of the bias magnetic field, macroscopic nonreciprocal entanglement is realized in this all-solid-state quantum system, which may find potential applications in chiral quantum information processing.

DOI: 10.1103/PhysRevApplied.21.034061

I. INTRODUCTION

Quantum entanglement is an essential resource for various quantum technologies, including quantum teleportation, quantum communications, and quantum sensing [1–4]. In particular, macroscopic quantum entanglement plays a crucial role in probing the boundary between the quantum and classical worlds [5–8], tests of decoherence theories at large mass scales [9,10], and gravitational quantum physics [11], among many others. Recently, magnons, the quanta of spin waves in magnetic materials, have attracted significant attention due to their high spin density, low damping rate, and great frequency tunability [12]. Therefore, they provide an ideal platform to realize macroscopic quantum entanglements including magnon-magnon [13–15], magnon-phonon [16,17], magnon-atomic ensemble [18–20], and others.

On the other hand, the nitrogen-vacancy-center ensemble (NVE) is another solid-state quantum system suitable for the study of macroscopic quantum effects. It possesses excellent spin properties [21,22], such as long spin-coherence time [23–25], quantum-state controllability [26,27], and the ability to initialize and read out the spin state optically [28,29]. Recent theoretical and experimental research has revealed the coupling of magnons in microscopic magnets to nitrogen-vacancy (N-V) centers in diamond [30–34]. However, previous studies have mostly focused on the interactions between the single N-V spin and the magnon. In comparison to a single N-V spin, the NVE is more suitable for storing local quantum information [21]. This stems from the fact that the collective interaction between NVEs and light fields is enhanced by increasing the spin numbers, and the long-lived coherence contained in the spin ensemble assumes a pivotal role in the realization of high-fidelity quantum memories. So far, numerous schemes have been presented for the preparation of NVE-NVE entanglement based on quantum state manipulation [35–37], quantum reservoir engineering [38,39], N-V–nanotube coupling [40], initial squeezing [41], and so on. Yet, the hybrid entanglement between magnons and NVEs remains underexplored territory, despite its potential applications in the construction of solid-state quantum information processors.

Nonreciprocal devices that break time-reversal symmetry are essential building blocks for information processing and sensing [42]. In recent years, the one-way flow of classical information has been extensively studied by using synthetic materials [43–48], solid devices [49–55], atoms [56,57], and so on. Significant advancements have also been achieved in the practical applications of nonreciprocity, including the development of nonreciprocal phonon laser [58,59], nonreciprocal nanoparticle sensing [60,61], nonreciprocal slow light [62,63], and nonreciprocal optical solitons [64]. Simultaneously, substantial progress has been made in nonreciprocal quantum effects. One-way quantum blockade [65–69], single-photon diodes [70,71], and nonreciprocal entanglement [72–77] and steering [78,79] have been explored theoretically, and nonreciprocal photon pairs [80] and cavity polaritonics [81] have been experimentally confirmed. These findings cast a profound illumination on the intersection of nonreciprocal physics and quantum technology, heralding a host of innovative applications. Particularly noteworthy is nonreciprocal entanglement, which is robustly protected by the breaking

*Corresponding author: feiwang@hbut.edu.cn

of Lorentz reciprocity [72]. This advancement holds significant promise for chiral sensing, chiral quantum information processing, and constructing chiral quantum networks, representing a notable stride forward in the evolution of quantum technologies [82].

In this paper, we propose a scheme for generating nonreciprocal entanglement between magnons and NVEs via the magnon Kerr effect. We employ a pair of NVEs and an yttrium iron garnet (YIG) sphere to interact with a transmission-line resonator (TLR) simultaneously. Under the assumption that both NVEs operate in the low-excitation limit, we can treat the collective variables as two bosonic fields using the Holstein-Primakoff approximation [83]. By operating in the dispersive regime, the TLR serves as a quantum bus, and the magnon-NVE and NVE-NVE couplings are realized via exchanging virtual photons [84–87]. We demonstrate that bipartite magnon-NVE entanglement, NVE-NVE entanglement, and tripartite entanglement can be nonreciprocally established. Moreover, the internal mechanisms to interpret the origin of the nonreciprocal entanglements are attributed to the magnon parametric amplifier (MPA) and magnon frequency shift (MFS) hidden behind magnon Kerr effects. Specifically, MPA initially prepares the magnon mode into a squeezed state, which is then mapped into the two NVE bosonic modes through beam-splitter interaction. The Kerr-effect-induced MFS, similar to the Sagnac effect in the cavity field, can be switched from positive to negative by changing the direction of the magnetic field. This modulates the optimal positions for all entanglements, resulting in nonreciprocity.

In comparison with previous studies on nonreciprocal entanglement [72–77], our scheme exhibits the following advantages: (i) Previous proposals mostly relied on the Sagnac effect for inducing nonreciprocity, achieved by driving spinning cavities along different directions to generate opposite frequency shifts. In contrast, our approach exploits the magnon-Kerr-effect-induced MFS, which depends on the direction of the bias magnetic field, providing an alternative way for exploring nonreciprocal quantum effects. (ii) Unlike prior methods necessitating radiation pressure interactions for generating entanglement, our scheme only requires the standard beam-splitter interaction and the entanglement arises exclusively from the magnon-Kerr-effect-induced MPA, eliminating the necessity for complex interactions or external nonlinear inputs. (iii) More importantly, the system utilized in the present scheme is all-solid-state characterized by robust scalability and operability. It performs well even under bad-cavity conditions, owing to the interactions being virtual-photon processes. This makes it more applicable to current laboratory techniques.

The remaining part of this paper is organized as follows. In Sec. II, we describe the model and equations of our scheme. In Sec. III, we present the physical mechanisms and then perform the numerical verification for the nonreciprocal entanglements. The paper ends with a conclusion in Sec. IV.

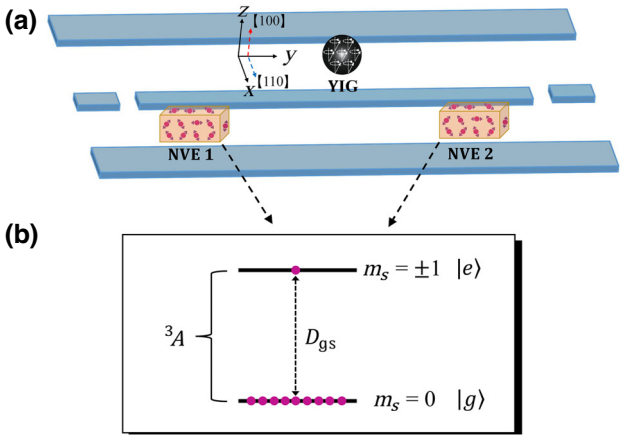

FIG. 1. (a) Sketch of the hybrid quantum system. Two NVEs and a YIG sphere are installed in a TLR cavity. The cavity magnetic field is along the y direction and coupled to the magnon and NVEs. The static bias magnetic field $\mathbf{B}_0$ is applied locally to the YIG sphere along the z direction. Superconducting microwave coils with a small loop antenna are mounted behind the YIG sphere to directly drive the magnon mode along the x direction (with Rabi frequency Ω_m). (b) Level structure of a single N-V center, where $D_{gs}/2\pi = 2.87$ GHz is the zero-field splitting between the lowest energy sublevels $|m_s = 0\rangle$ and $|m_s = \pm 1\rangle$.

II. MODEL AND EQUATIONS

As shown in Fig. 1(a), two NVEs and a YIG sphere are dispersively coupled with a TLR cavity, in which the TLR serves as a quantum bus mediating effective coupling between objects in the cavity. The NVE consists of $N = 10^{12}$ N-V centers in a diamond crystal. Each N-V center is negatively charged with two unpaired electrons located at the vacancy, which can be modeled as a two-level system in the ground subspaces. As shown in Fig. 1(b), the electronic ground states of the single N-V center are spin triplet states, labeled ^3A. There is a zero-field splitting $D_{gs}/2\pi = 2.87$ GHz between the degenerate sublevels $|m_s = \pm 1\rangle$ and $|m_s = 0\rangle$ [21,22]. For simplicity, we consider the ground state $|m_s = 0\rangle = |g\rangle$ and the excited state $|m_s = \pm 1\rangle = |e\rangle$. In addition, the YIG sphere is saturated magnetized by a uniform magnetic field $\mathbf{B}_0$ [88]. Meanwhile, we consider the strong and tunable magnon Kerr effect, originating from the magnetocrystalline anisotropy in the YIG sphere and being demonstrated by recent experiments [89–91]. Generally, to enhance the magnon Kerr effect, the YIG sphere should be driven by a superconducting microwave line with a small loop antenna [92,93].

The Hamiltonian for the whole system reads (taking $\hbar = 1$)

$$H = H_c + H_n + H_m + H_d + H_I. \tag{1}$$

Here the first term $H_c = \omega_c a^\dagger a$ describes the free Hamiltonian of the TLR cavity mode, with a ($a^\dagger$) being the annihilation (creation) operator of the cavity field at frequency ω_c. The second term

$$H_n = \sum_{l=1,2} \omega_n \sigma_l^\dagger \sigma_l \tag{2}$$

represents the Hamiltonian of the NVEs, where $\sigma_l = \sum_{\mu=1}^{N} |g_l\rangle_\mu \langle e_l|$ are the collective spin-flip operators of the lth ensemble ($l = 1, 2$), where $|g_l\rangle$ and $|e_l\rangle$ are the ground and excited states, respectively, with resonant transition frequency $\omega_n = D_{\rm gs}$.

The third term has the form

$$H_m = -\gamma_0 B_0 S_z + D_x S_x^2 + D_y S_y^2 + D_z S_z^2, \tag{3}$$

which is used to describe the Zeeman energy, the magnetocrystalline anisotropy energy (see Appendix A) [92,93]. Here, $\gamma_0 = 28$ GHz/T is the gyromagnetic ratio, the nonlinear coefficients D_i rely on the crystallographic axis of the YIG sphere, along which the bias magnetic field $\mathbf{B}_0$ is applied, and $\mathbf{S} = (S_x, S_y, S_z)$ stands for the collective spin operator. When the different crystallographic axes [100] or [110] are aligned along the biased magnetic field $\mathbf{B}_0$, the nonlinear coefficients D_i will be expressed differently (the detailed derivation is given in Appendix A)

$$\begin{aligned} &D_x = 0, \quad D_y = 0, \quad D_z = \frac{\mu_0 K_{\rm an} \gamma_0^2}{M^2 V_m}, && \text{for [100]}, \\ &D_x = 3D_z, \quad D_y = \frac{9}{4} D_z, \quad D_z = \frac{\mu_0 K_{\rm an} \gamma_0^2}{2M^2 V_m}, && \text{for [110]}, \end{aligned} \tag{4}$$

where $K_{\rm an}$ (> 0) is the first-order anisotropy constant of the YIG, M is the saturation magnetization, V_m is the volume of the YIG sphere, and μ_0 is the vacuum permeability.

The fourth term, the interaction between the macrospin and the drive field, is

$$H_d = \Omega_s (S_+ e^{i\omega_p t} + S_- e^{-i\omega_p t}), \tag{5}$$

where $S_\pm = S_x \pm i S_y$ are, respectively, the raising and lowering operators of the macrospin in the YIG sphere, and $\Omega_s = \mu_0 \gamma_0 B_d / 4$ denotes the coupling strength between each single spin and the driving field with amplitude B_d and frequency ω_p. Finally, the fifth term, the interaction Hamiltonian describing the NVEs and the YIG sphere coupled to the TLR, can be written as

$$H_I = g_n a (\sigma_1^\dagger + \sigma_2^\dagger) + g_s a S_- + \text{H.c.}, \tag{6}$$

where g_n and g_s represent the coupling strengths associated with the interaction of the cavity field with the NVEs and the macrospin of the YIG sphere, respectively.

The macrospin operators of the YIG sphere are related to the magnon operators via the Holstein-Primakoff transformation [83], $S_+ = (\sqrt{2S - m^\dagger m})m$, $S_- = m^\dagger(\sqrt{2S - m^\dagger m})$, and $S_z = S - m^\dagger m$, where $S = 5\rho V_m/2$ is the total spin number in the YIG sphere with spin density $\rho = 4.22 \times 10^{27}$ m^{-3} [17], and $m^\dagger$ (m) denotes the creation (annihilation) operator of the magnon. For the low-lying magnon excitations with $\langle m^\dagger m \rangle \ll 2S$, one has $S_+ = m\sqrt{2S}$ and $S_- = m^\dagger \sqrt{2S}$. Similarly, we assume that the NVEs are initially prepared in the ground state, and that they are in the low-excitation limit.

In this case, we can also adopt the Holstein-Primakoff approximation [83] to describe the NVEs as two bosonic modes $b_l = \sigma_l / \sqrt{N}$ satisfying $[b_l, b_l^\dagger] = 1$. Then, we obtain the fully bosonized Hamiltonian

$$\begin{aligned} H = {} & \omega_c a^\dagger a + \omega_n (b_1^\dagger b_1 + b_2^\dagger b_2) + \omega_m m^\dagger m + \mathcal{K} m^\dagger m m^\dagger m \\ & + g_b (a b_1^\dagger + a^\dagger b_1 + a b_2^\dagger + a^\dagger b_2) + g_m (a m^\dagger + a^\dagger m) \\ & + \Omega_m (m e^{-i\omega_p t} + m^\dagger e^{i\omega_p t}), \end{aligned} \tag{7}$$

where the frequency of magnon mode ω_m and the Kerr nonlinear coefficient $\mathcal{K}$ also have the distinct expressions

$$\begin{aligned} &\omega_m = \gamma_0 B_0 - \frac{2\mu_0 K_{\rm an} \gamma_0^2 S}{M^2 V_m}, \quad \mathcal{K} = \frac{\mu_0 K_{\rm an} \gamma_0^2}{M^2 V_m}, && \text{for [100]}, \\ &\omega_m = \gamma_0 B_0 + \frac{13\mu_0 K_{\rm an} \gamma_0^2 S}{8M^2 V_m}, \mathcal{K} = -\frac{13\mu_0 K_{\rm an} \gamma_0^2}{16 M^2 V_m}, && \text{for [110]}, \end{aligned} \tag{8}$$

for different crystallographic axes [100] or [110] of the YIG sphere along the bias magnetic field. Now, it becomes evident that by adjusting the direction of the biased magnetic field, the Kerr coefficient can be either positive ($\mathcal{K} > 0$) or negative ($\mathcal{K} < 0$). In the above, $g_b = g_n\sqrt{N}$ and $g_m = g_s\sqrt{2S}$ are the effective cavity-NVE and cavity-magnon coupling strengths, and $\Omega_m = \Omega_s\sqrt{2S}$ is the Rabi frequency of the driving field applied to the magnons.

In the rotating frame $H_r = \omega_c a^\dagger a + \omega_p (b_1^\dagger b_1 + b_2^\dagger b_2 + m^\dagger m)$, the total Hamiltonian can be written as

$$\begin{aligned} H = {} & \Delta_n' (b_1^\dagger b_1 + b_2^\dagger b_2) + \Delta_m' m^\dagger m + \mathcal{K} m^\dagger m m^\dagger m \\ & + [g_b (a b_1^\dagger + a b_2^\dagger) e^{i\Delta t} + g_m a m^\dagger e^{i\Delta t} + \text{H.c.}] \\ & + \Omega_m (m + m^\dagger). \end{aligned} \tag{9}$$

Here $\Delta_n' = \omega_n - \omega_p$, $\Delta_m' = \omega_m - \omega_p$, and $\Delta = \omega_c - \omega_p$ are the frequency detunings of NVE, magnon, and cavity with respect to the driving field, respectively. In the case of $\Delta \gg \Delta_n', \Delta_m', \mathcal{K}, g_b, g_m$, the cavity mode is virtually excited [84–87]. Then the effective Hamiltonian is

given by

$$H_{\text{eff}} = \Delta_n(b_1^\dagger b_1 + b_2^\dagger b_2) + \Delta_m m^\dagger m + \mathcal{K} m^\dagger m m^\dagger m + [g_1 m(b_1^\dagger + b_2^\dagger) + g_2 b_1 b_2^\dagger + \Omega_m m + \text{H.c.}], \quad (10)$$

with $g_1 = g_b g_m/\Delta$, $g_2 = g_b^2/\Delta$, $\Delta_n = \Delta_n' + g_b^2/\Delta$, and $\Delta_m = \Delta_m' + g_m^2/\Delta$. It can be seen that coherent magnon-NVE together with NVE-NVE interactions are induced by the exchange of virtual photons.

The master equation for the density operator ρ of the effective magnon-NVE coupled system is written as [94, 95]

$$\frac{d}{dt}\rho = -i[H_{\text{eff}}, \rho] + \gamma \sum_{l=1}^{2} \mathcal{L}_{b_l}\rho + \kappa_m(n_{\text{th}} + 1)\mathcal{L}_m\rho + \kappa_m n_{\text{th}}\mathcal{L}_{m^\dagger}\rho, \quad (11)$$

where $\mathcal{L}_o\rho$ $(o = m, b_1, b_2)$ takes the standard form $\mathcal{L}_o\rho = \frac{1}{2}(2o\rho o^\dagger - o^\dagger o\rho - \rho o^\dagger o)$, describing the damping of the NVEs and magnon with rates γ and κ_m, respectively, and $n_{\text{th}} = [\exp(\hbar\omega_m/k_B T) - 1]^{-1}$ being the equilibrium thermal magnon occupation number, with the Boltzmann constant k_B and the ambient temperature T.

Following the standard technique [96], the dissipative dynamics of the system can be described by a set of quantum Langevin equations (QLEs):

$$\begin{aligned}
\dot{m} &= -\left(\frac{\kappa_m}{2} + i\Delta_m\right) m - i2\mathcal{K} m^\dagger m m - ig_1(b_1 + b_2) + \Omega_m + \sqrt{\kappa_m}m^{\text{in}}, \\
\dot{b}_1 &= -\left(\frac{\gamma}{2} + i\Delta_n\right) b_1 - ig_1 m - ig_2 b_2 + \sqrt{\gamma}b_1^{\text{in}}, \\
\dot{b}_2 &= -\left(\frac{\gamma}{2} + i\Delta_n\right) b_2 - ig_1 m - ig_2 b_1 + \sqrt{\gamma}b_2^{\text{in}}, \quad (12)
\end{aligned}$$

wherein m^{in} and b_l^{in} are noise operators for the magnon and NVEs, respectively, with zero means and characterized by the nonvanishing correlation functions: $\langle m^{\text{in}}(t)m^{\dagger\text{in}}(t')\rangle = (n_{\text{th}} + 1)\delta(t - t')$, $\langle m^{\dagger\text{in}}(t)m^{\text{in}}(t')\rangle = n_{\text{th}}\delta(t - t')$ and $\langle b_l^{\text{in}}(t)b_l^{\dagger\text{in}}(t')\rangle = \delta(t - t')$.

Since the magnon is under strong driving, leading to a large amplitude $|\langle m\rangle| \gg 1$, and further owing to the effective magnon-NVE beam-splitter-like interactions, the two bosonic modes of NVEs are also of large amplitudes. This allows us to linearize the system dynamics by introducing the expansion $o = \langle o\rangle + \delta o$, and neglecting small second-order fluctuation terms. Substituting those linearized operators into Eq. (12), we can obtain two sets of equations, one of semiclassical averages and the other of quantum fluctuations. By solving the semiclassical equations, the solutions of the averages are obtained

$$\begin{aligned}
\langle m\rangle &= \frac{2\Omega_m(\gamma + 2i\delta_n)}{(\gamma + 2i\delta_n)(\kappa_m + 2i\delta_m) + 8g_1^2}, \\
\langle b_1\rangle &= \langle b_2\rangle = \frac{-2ig_1\langle m\rangle}{\gamma + 2i\delta_n}, \quad (13)
\end{aligned}$$

where $\delta_n = \Delta_n + g_2$ and $\delta_m = \Delta_m + 2\mathcal{K}|\langle m\rangle|^2$. For simplicity, $\langle m\rangle$ is assumed to be real via properly choosing the phase of the driving field.

In order to investigate quantum entanglement, we define a pair of quadrature operators of quantum fluctuations as $X_o = \frac{1}{\sqrt{2}}(\delta o + \delta o^\dagger)$ and $P_o = -i/\sqrt{2}(\delta o - \delta o^\dagger)$. Meanwhile, the noise quadratures X_o^{in} and P_o^{in} are defined in the same way. The QLEs describing the quadrature fluctuations can be written as

$$\dot{u}(t) = Au(t) + \xi(t), \quad (14)$$

where the column vector for the fluctuation variables is arranged as $u(t) = (X_m, P_m, X_{b_1}, P_{b_1}, X_{b_2}, P_{b_2})^T$, the corresponding noise terms are listed as $\xi(t) = (X_m^{\text{in}}, P_m^{\text{in}}, X_{b_1}^{\text{in}}, P_{b_1}^{\text{in}}, X_{b_2}^{\text{in}}, P_{b_2}^{\text{in}})^T$, and the drift matrix reads as

$$A = \begin{pmatrix}
-\kappa_m/2 & \widetilde{\Delta}_m - 2\widetilde{\mathcal{K}} & 0 & g_1 & 0 & g_1 \\
-(\widetilde{\Delta}_m + 2\widetilde{\mathcal{K}}) & -\kappa_m/2 & -g_1 & 0 & -g_1 & 0 \\
0 & g_1 & -\gamma/2 & \Delta_n & 0 & g_2 \\
-g_1 & 0 & -\Delta_n & -\gamma/2 & -g_2 & 0 \\
0 & g_1 & 0 & g_2 & -\gamma/2 & \Delta_n \\
-g_1 & 0 & -g_2 & 0 & -\Delta_n & -\gamma/2
\end{pmatrix}, \quad (15)$$

where $\widetilde{\Delta}_m = \Delta_m + 4\widetilde{\mathcal{K}}$ is the effective detuning, and $\widetilde{\mathcal{K}} = \mathcal{K}|\langle m\rangle|^2$ is the strength of the magnon parametric amplifier. As the sign of $\mathcal{K}$ can be tuned, we have $\widetilde{\mathcal{K}} > 0$ or $\widetilde{\mathcal{K}} < 0$ for the case with the crystallographic axis [100] or [110] along the bias magnetic field, and the corresponding effective detuning experiences an opposite shift. According to the Routh-Hurwitz criterion [97], it is easy to verify that, if all eigenvalues of the drift matrix A have negative real parts, then the system is stable (see Appendix B for details).

In the present work, we mainly focus on the quantum correlations in the steady state. The system will decay to a stationary Gaussian state that can be characterized by a 6×6 covariance matrix (CM) C whose matrix element is defined by $C_{ij}(t,t') = \frac{1}{2}\langle u_i(t)u_j(t') + u_j(t')u_i(t)\rangle$ $(i,j = 1,2,\ldots,6)$. The steady-state CM can be obtained straightforwardly by solving the Lyapunov equation [98, 99]

$$AC + CA^T = -D, \tag{16}$$

with the diffusion matrix $D = \mathrm{diag}[\kappa_m(2n_{\mathrm{th}}+1), \kappa_m(2n_{\mathrm{th}}+1), \gamma, \gamma, \gamma, \gamma]/2$. The diffusion matrix D is defined through $D_{ij}\,\delta(t-t') = \frac{1}{2}\langle \xi_i(t)\xi_j(t') + \xi_j(t')\xi_i(t)\rangle$.

To study the magnon-NVE and NVE-NVE bipartite entanglements, we adopt the logarithmic negativity E_N by computing the 6×6 CM related to the two modes of interest [100,101]. The logarithmic negativity for Gaussian states is defined as

$$E_N = \max[0, -\ln 2v], \tag{17}$$

where $v = \min \mathrm{eig}|\bigoplus_{j=1}^{2} -(\sigma_y)\mathcal{P}\mathcal{C}_4\mathcal{P}|$ denotes the minimum symplectic eigenvalue, for which σ_y is the y Pauli matrix, $\mathcal{C}_4$ is the 4×4 CM of the two subsystems that include only the rows and columns of the modes of interest in C, and $\mathcal{P} = \sigma_z \oplus 1$ is the matrix that realizes partial transposition at the level of the CM.

The magnon-NVE tripartite entanglement is quantified by the *minimum residual contangle* [102] defined as

$$\mathcal{R}_{i|jk} = C_{i|jk} - C_{i|j} - C_{i|k}. \tag{18}$$

Here $C_{u|v}$ is the contangle of subsystems u and v (v may involve one or two modes). This is a proper entanglement monotone defined as the squared logarithmic negativity, i.e., $C_{u|v} = E_{u|v}^2$. The *one-mode-versus-two-modes* logarithmic negativity $E_{i|jk} = \max[0, -\ln 2v_{i|jk}]$, where $v_{i|jk} = \min \mathrm{eig}|\bigoplus_{j=1}^{3} -(\sigma_y)\mathcal{P}_{i|jk}\mathcal{C}\mathcal{P}_{i|jk}|$ with $\mathcal{P}_{1|23} = \sigma_z \oplus 1 \oplus 1$, $\mathcal{P}_{2|13} = 1 \oplus \sigma_z \oplus 1$, and $\mathcal{P}_{3|12} = 1 \oplus 1 \oplus \sigma_z$ being the matrices for partial transposition at the level of the 6×6 CM. The residual contangle satisfies the monogamy of quantum entanglement, i.e., $\mathcal{R}_{i|jk} \geq 0$, which is similar of the Coffman-Kundu-Wootters monogamy inequality in Ref. [103]. A *bona fide* quantification of tripartite entanglement for Gaussian states is given by the minimum residual contangle

$$\mathcal{R}_{\min} = \min[\mathcal{R}_{m|b_1b_2}, \mathcal{R}_{b_1|mb_2}, \mathcal{R}_{b_2|mb_1}], \tag{19}$$

which guarantees the invariance of tripartite entanglement under all permutations of the modes.

III. ANALYSIS AND DISCUSSION

A. Physical mechanism

Before studying entanglement, it is necessary to elucidate the mechanism for the nonreciprocal entanglement induced by Kerr nonlinearities. Specifically, the magnon Kerr effect not only generates an MPA process, but also gives a red or blue MFS. The former is the source of entanglement, while the latter will induce the nonreciprocity of the system.

Firstly, following the standard linearization treatment, we can obtain the linearized Hamiltonian for quantum fluctuations:

$$\begin{aligned} H_{\mathrm{lin}} = {} & \Delta_n(\delta b_1^\dagger \delta b_1 + \delta b_2^\dagger \delta b_2) + \widetilde{\Delta}_m \delta m^\dagger \delta m + \widetilde{\mathcal{K}}(\delta m^2 \\ & + \delta m^{\dagger 2}) + [g_1 \delta m(\delta b_1^\dagger + \delta b_2^\dagger) + g_2 \delta b_1 \delta b_2^\dagger + \mathrm{H.c.}]. \end{aligned} \tag{20}$$

Now it is seen from the linearized Hamiltonian, Eq. (20), that the magnon Kerr nonlinearities can be equivalent to an MPA process, which is responsible for the magnon squeezing. Then, to elaborate the mechanism of entanglement, we introduce two collective NVE modes as $\delta b_+ = (1/\sqrt{2})(\delta b_1 + \delta b_2)$ and $\delta b_- = (1/\sqrt{2})(\delta b_1 - \delta b_2)$. Here the new operators satisfy the bosonic commutation relations $[\delta b_+, \delta b_+^\dagger] = 1$ and $[\delta b_-, \delta b_-^\dagger] = 1$. By substituting the operators $\delta b_\pm$ ($b_\pm^\dagger$) into Eq. (20), the Hamiltonian can be rewritten as

$$\begin{aligned} H'_{\mathrm{lin}} = {} & (\Delta_n + g_2)\delta b_+^\dagger \delta b_+ + (\Delta_n - g_2)\delta b_-^\dagger \delta b_- \\ & + \widetilde{\Delta}_m \delta m^\dagger \delta m + \widetilde{\mathcal{K}}(\delta m^2 + \delta m^{\dagger 2}) + \frac{g_1}{\sqrt{2}} \\ & \times (\delta m \delta b_+^\dagger + \delta m^\dagger \delta b_+). \end{aligned} \tag{21}$$

Obviously, only the NVE bright mode δb_+ appears in the interaction term of Eq. (21) while the mode δb_- decouples from the magnon mode δm, which means that the mode δb_- becomes a dark mode.

Physically, the first three terms in Eq. (21) are free Hamiltonians for the collective modes and magnon mode, respectively. The fourth term is referred to as the MPA process with effective strength $\widetilde{\mathcal{K}}$ and the last term is responsible for the transfer process between bright mode δb_+ and magnon mode δm.

It is well known that the MPA leads to magnon squeezing, and the beam-splitter interactions result in the transfer of quantum states. When $\Delta_n + g_2 = -\widetilde{\Delta}_m$ (i.e., $\Delta_m = -(\Delta_n + g_2) - 4\widetilde{\mathcal{K}}$), MPAs squeeze the magnon mode and, simultaneously, the quantum state of the magnon mode δm transfers to the NVE bright mode δb_+ by the beam-splitter interactions. This process gives rise to the generation of optimal magnon-NVE entanglement. Interestingly, we note that the entanglement is enhanced with decreasing of

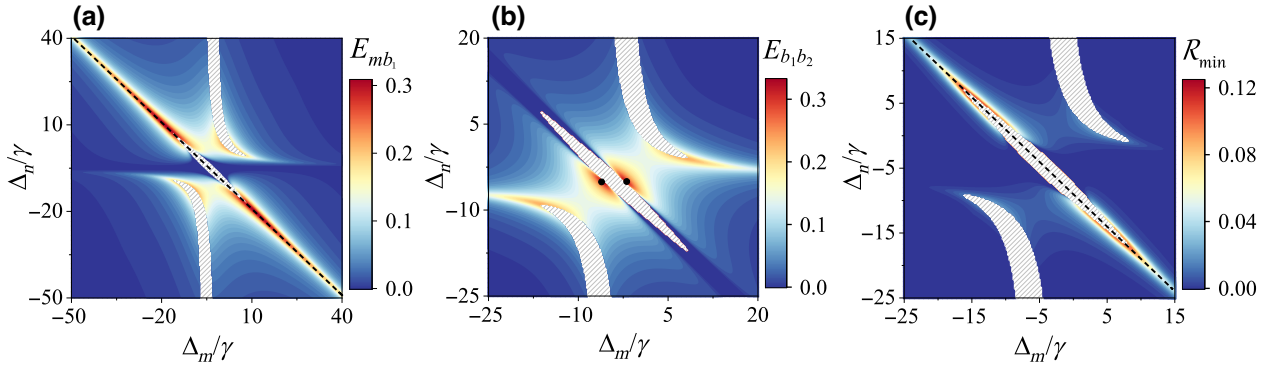

FIG. 2. Density plots of (a) magnon-NVE bipartite entanglement E_{mb_1}, (b) NVE-NVE bipartite entanglement $E_{b_1b_2}$, and (c) magnon-NVE tripartite entanglement $\mathcal{R}_{\min}$ versus detunings Δ_n and $\widetilde{\Delta}_m$. The black dashed lines in panels (a) and (c) indicate the condition $\Delta_m = -(\Delta_n + g_2) - 4\widetilde{\mathcal{K}}$, while the two black dots in panel (b) indicate the condition $\Delta_n = -g_2$ and $\Delta_m = -2\widetilde{\mathcal{K}}, -6\widetilde{\mathcal{K}}$. The other parameters are chosen as $\omega_m = 10$ GHz, $\gamma/2\pi = \kappa_m/2\pi = 0.1$ MHz, $\widetilde{\mathcal{K}} = \gamma$, $g_1 = g_2 = g = 5\gamma$, and $T = 50$ mK. The gray areas show the unstable region, and the blue areas represent the areas where entanglement does not exist.

$|\widetilde{\Delta}_m|$ (i.e., $|\Delta_m + 4\widetilde{\mathcal{K}}|$) under the optimal detuning condition of $\Delta_n + g_2 = -\widetilde{\Delta}_m$. This can be attributed to the fact that the MPA and the beam-splitter interaction will play a remarkable role in generating entanglement when smaller $|\widetilde{\Delta}_m|$ is taken. By tuning the direction of the bias magnetic field, the optimal detuning condition $\Delta_m = -(\Delta_n + g_2) - 4\widetilde{\mathcal{K}}$ moves in the opposite direction for $\widetilde{\mathcal{K}} > 0$ or $\widetilde{\mathcal{K}} < 0$. Therefore, nonreciprocal magnon-NVE entanglement can be achieved.

On the other hand, in order to understand the essential origin of the optimal NVE-NVE entanglement, we operate the system in the squeezed-magnon frame via the Bogoliubov transform $\delta m = \delta m_s \cosh r + \delta m_s^\dagger \sinh r$ and $\delta m^\dagger = \delta m_s \sinh r + \delta m_s^\dagger \cosh r$ [94,95]. Substituting this expression into Eq. (21), and setting the squeezing parameter $r = (1/4)\ln[(\widetilde{\Delta}_m - 2\widetilde{\mathcal{K}})/(\widetilde{\Delta}_m + 2\widetilde{\mathcal{K}})]$, we can reduce Eq. (21) to

$$\begin{aligned} H_{\rm lin}'' = {} & (\Delta_n + g_2)\delta b_+^\dagger \delta b_+ + (\Delta_n - g_2)\delta b_-^\dagger \delta b_- \\ & + \Delta_s \delta m_s^\dagger \delta m_s + \frac{g_1}{\sqrt{2}}[\sinh r\, \delta m_s \delta b_+ \\ & + \cosh r\, \delta m_s \delta b_+^\dagger + \text{H.c.}], \end{aligned} \tag{22}$$

with $\Delta_s = \sqrt{\widetilde{\Delta}_m^2 - 4\widetilde{\mathcal{K}}^2}$.

Obviously, we can see that both parametric and beam-splitter interactions coexist between the squeezed magnon mode δm_s and the NVE bright mode δb_+. When $\Delta_n + g_2 = \Delta_s = 0$ (i.e., $\Delta_n = -g_2$ and $\Delta_m = -2\widetilde{\mathcal{K}}, -6\widetilde{\mathcal{K}}$), the squeezing parameter $|r| \to \infty$, and the parametric and beam-splitter interactions are exponentially enhanced [104,105]. At this time, the NVE bright mode δb_+ first entangles with the squeezed magnon mode δm_s and then the entanglement transfers back to itself, resulting in the appearance of optimal NVE-NVE entanglement. Similarly, manipulating the parameter $\widetilde{\mathcal{K}}$ to assume negative or positive values—effectively altering the direction of the bias magnetic field—results in distinctive responses in the optimal NVE-NVE entanglement. This tunability introduces a nonreciprocal behavior, illustrating the sensitivity of the system to the directional orientation of the bias magnetic field.

In order to verify the validity of the above theoretical analysis, we plot the bipartite and tripartite entanglements as functions of the detunings Δ_n and Δ_m, as shown in Fig. 2. Since two NVEs are assumed to be identical, we have the relation $E_{mb_1} = E_{mb_2}$. Here we have taken into account the parameters as in Refs. [89–91], i.e., $\omega_m/2\pi = 10$ GHz, $\gamma/2\pi = \kappa_m/2\pi = 0.1$ MHz, $g_1 = g_2 = g = 5\gamma$, $\widetilde{\mathcal{K}} = \gamma$, and $T = 50$ mK. In Fig. 2(a), it is seen that the strong magnon-NVE entanglement E_{mb_1} appears in the regime near the condition $\Delta_m = -(\Delta_n + g_2) - 4\widetilde{\mathcal{K}}$, and increases accompanied by the reduction of $|\Delta_m|$ in the stable region. The above phenomena are in good agreement with the theoretical analysis in the Hamiltonian (21). As shown in Fig. 2(b), the strong NVE-NVE entanglement $E_{b_1b_2}$ occurs around $\Delta_n = -g_2$ and $\Delta_m = -2\widetilde{\mathcal{K}}, -6\widetilde{\mathcal{K}}$, which proves the validity of the physical analysis in the Hamiltonian (22). From Fig. 2(c), we find that the tripartite entanglement is obtained under the same conditions as the optimal magnon-NVE bipartite entanglement, but it only appears in the region where an NVE mode and the magnon mode are strongly entangled. Moreover, it is worth mentioning that the tripartite entanglement in the present scheme is much stronger than those reported in previous schemes [17,106].

B. Nonreciprocal bipartite and tripartite entanglements

In the following discussion, we will demonstrate how to achieve nonreciprocal entanglement within our system. We underscore the pivotal role of the magnon Kerr effect

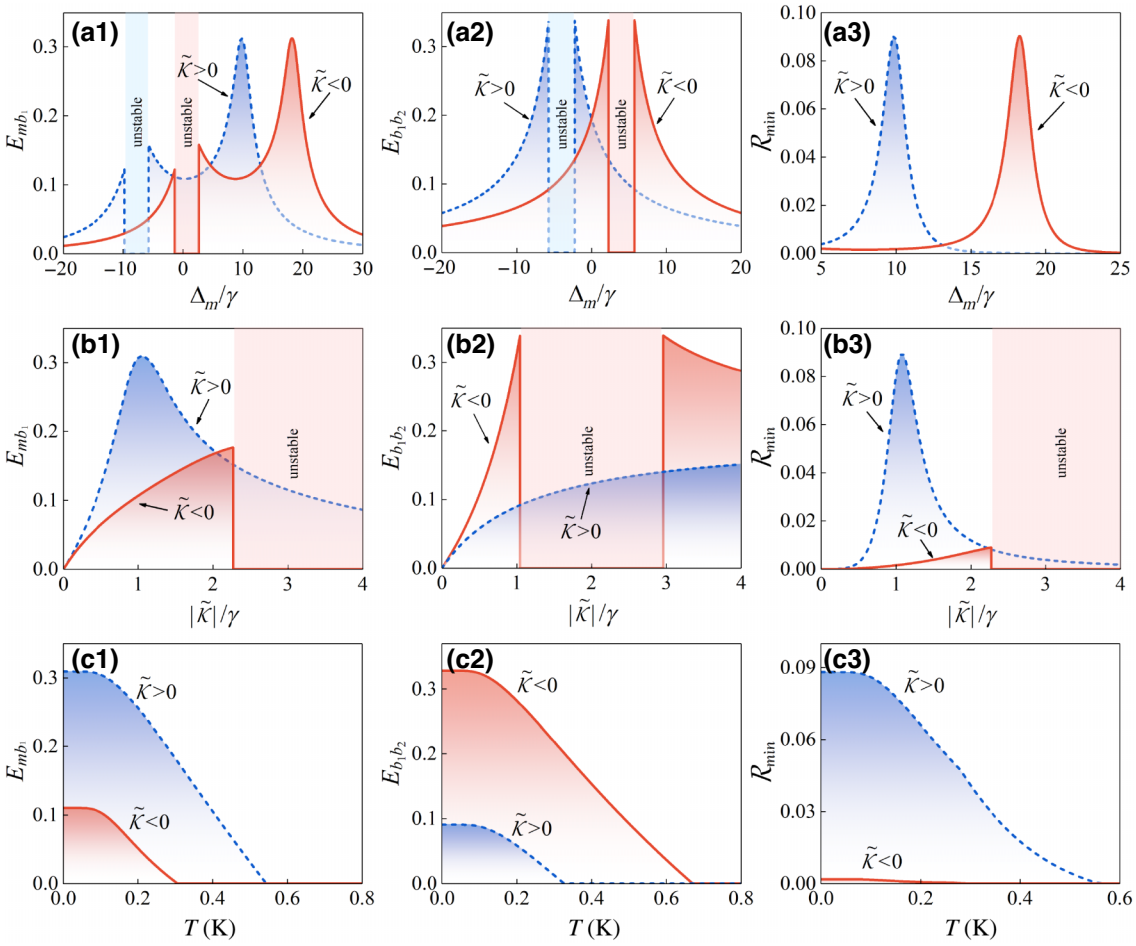

FIG. 3. Bipartite entanglements E_{mb_1} (left) and $E_{b_1b_2}$ (middle), and tripartite entanglement $\mathcal{R}_{\min}$ (right) versus the detuning Δ_m (top), strength of MPA $|\widetilde{\mathcal{K}}|$ (middle), and ambient temperature T (bottom), respectively. The solid red and the dashed blue lines, respectively, denote $\widetilde{\mathcal{K}} < 0$ and $\widetilde{\mathcal{K}} > 0$, and the red and blue shaded areas show the corresponding unstable regions. We take $\Delta_n = -19\gamma$ in (a1) and (a3); $\Delta_n = -5\gamma$ in (a2); $\Delta_n = -19\gamma$ and $\Delta_m = 10\gamma$ in (b1), (b3), (c1), and (c3); and $\Delta_n = -5\gamma$ and $\Delta_m = 6\gamma$ in (b2) and (c2). The other parameters are the same as in Fig. 2.

in the preparation of nonreciprocal entanglement, given its capacity to induce both the MPA and the MFS. Specifically, the MPA contributes to entanglement generation, while the MFS is crucial for the emergence of nonreciprocity. Importantly, the direction of the applied magnetic field dictates these phenomena.

To investigate nonreciprocal entanglements, we plot bipartite and tripartite entanglements versus the magnon frequency detuning Δ_m in Figs. 3(a1)–3(a3). The solid red and the dashed blue lines, respectively, denote the magnetic field along the crystalline axis [110] and [100], corresponding to the two cases of $\widetilde{\mathcal{K}} < 0$ and $\widetilde{\mathcal{K}} > 0$. From Fig. 3(a1), we find the maximal magnon-NVE bipartite entanglement, when the magnon detuning $\Delta_m \approx 10\gamma$ for $\widetilde{\mathcal{K}} > 0$ and $\Delta_m \approx 18\gamma$ for $\widetilde{\mathcal{K}} < 0$. This is consistent with the optimal condition $\Delta_m = -(\Delta_n + g_2) - 4\widetilde{\mathcal{K}}$. As shown in Fig. 3(a2), strong NVE-NVE entanglement occurs near the detuning $\Delta_m \approx \pm 2\gamma, \pm 6\gamma$ for a fixed NVE detuning $\Delta_n = -g_2 = -5\gamma$, which perfectly match the optimal conditions of $\Delta_n = -g_2$ and $\Delta_m = -2\widetilde{\mathcal{K}}, -6\widetilde{\mathcal{K}}$ for $\widetilde{\mathcal{K}} < 0$ and $\widetilde{\mathcal{K}} > 0$. As expected, the optimal tripartite entanglement is generated at the same condition of magnon-NVE bipartite entanglement [see Fig. 3(a3)]. In addition, by tuning the direction of the magnetic field, i.e., changing the positive and negative of $\widetilde{\mathcal{K}}$, the optimal positions of all entanglements will have different responses. The different responses to magnetic field directions give rise to the emergence of nonreciprocal entanglement.

Moreover, it is of interest to discuss the effects of the MPA strength $|\widetilde{\mathcal{K}}|$ on the nonreciprocal entanglements. Figures 3(b1)–3(b3) illustrate bipartite entanglements E_{mb_1} and $E_{b_1b_2}$, and tripartite entanglement $\mathcal{R}_{\min}$ versus $|\widetilde{\mathcal{K}}|$. Here, we fix $\Delta_n = -19\gamma$ and $\Delta_m = 10\gamma$ in Figs. 3(b1) and 3(b3), and $\Delta_n = -5\gamma$ and $\Delta_m = 6\gamma$ in Fig. 3(b2). On the one hand, it is shown that all entanglements are strongly dependent on the MPA strength $|\widetilde{\mathcal{K}}|$. When $|\widetilde{\mathcal{K}}| = 0$, both

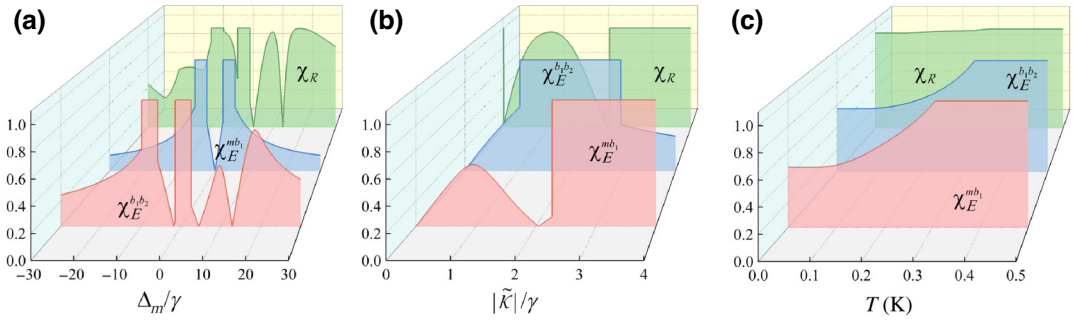

FIG. 4. Chiral factors for bipartite and tripartite entanglements as functions of (a) the detuning Δ_m, (b) the strength of MPA $|\tilde{\mathcal{K}}|$, and (c) temperature T. The other parameters are the same as in Fig. 3.

bipartite and tripartite entanglements are absent. This result reflects the fact that the MPA process is the source that produces all entanglements. On the other hand, for $\tilde{\mathcal{K}} > 0$ or $\tilde{\mathcal{K}} < 0$, all entanglements have completely different trends as $|\tilde{\mathcal{K}}|$ increases and the stability of the system responds differently. For example, Figs. 3(b1) and 3(b3) show that, when $\tilde{\mathcal{K}} > 0$, entanglements E_{mb_1} and $\mathcal{R}_{\min}$ first increase and then decrease as $|\tilde{\mathcal{K}}|$ increases, reaching an optimal value near $|\tilde{\mathcal{K}}| = \gamma$. This is because under the conditions of $\Delta_n = -19\gamma$, $\Delta_m = 10\gamma$, and $g_2 = 5\gamma$ the optimal magnon-NVE entanglement condition $\Delta_m = -(\Delta_n + g_2) - 4\tilde{\mathcal{K}}$ is satisfied only when $|\tilde{\mathcal{K}}| = \gamma$. However, when $\tilde{\mathcal{K}} < 0$, the obtained entanglements are weaker and the stable region of the system becomes smaller.

For $E_{b_1b_2}$ in Fig. 3(b2), we can see that the NVE-NVE entanglement reaches its maximum near $|\tilde{\mathcal{K}}| = \gamma, 3\gamma$ for $\tilde{\mathcal{K}} < 0$ and these two maximum values of entanglement are the same. The reason lies in the fact that the NVE-NVE entanglement arises from the parametric and beam-splitter interactions between the NVE bright mode and the squeezed magnon mode as shown in Hamiltonian (22), and the effective coupling strengths of these interactions are related to the magnon-NVE coupling strength g_1 and the squeezing parameter r. When the optimal detuning conditions $\Delta_n = -g_2$ and $\Delta_m = -2\tilde{\mathcal{K}}, -6\tilde{\mathcal{K}}$ are met, the effective coupling strengths reach their maximum, which remains unchanged with the increase of $|\tilde{\mathcal{K}}|$. In contrast, when $\tilde{\mathcal{K}} > 0$, the obtained NVE-NVE entanglement is weakened but the stable region becomes larger. The above phenomena demonstrate that the magnon Kerr effect is the root cause of nonreciprocal entanglement, which can be modulated by effectively regulating the strength of MPA.

As shown in Figs. 3(c1)–3(c3), we studied how the ambient temperature T affects nonreciprocal entanglements. Our findings show that, while the ambient temperature negatively impacts bipartite and tripartite entanglements, the obtained entanglements are relatively robust against environmental noise. Additionally, we discovered that all entanglements react differently to temperature in different cases ($\tilde{\mathcal{K}} > 0$ or $\tilde{\mathcal{K}} < 0$), which suggests a possible method for regulating the nonreciprocal entanglements.

To quantitatively describe the nonreciprocity of both bipartite and tripartite entanglements, we further introduce the chiral factors as follows [72,73,75–77]:

$$\chi_E^{ij} = \left| \frac{E_{ij}(\tilde{\mathcal{K}} > 0) - E_{ij}(\tilde{\mathcal{K}} < 0)}{E_{ij}(\tilde{\mathcal{K}} > 0) + E_{ij}(\tilde{\mathcal{K}} < 0)} \right|,$$
$$\chi_{\mathcal{R}} = \left| \frac{\mathcal{R}_{\min}(\tilde{\mathcal{K}} > 0) - \mathcal{R}_{\min}(\tilde{\mathcal{K}} < 0)}{\mathcal{R}_{\min}(\tilde{\mathcal{K}} > 0) + \mathcal{R}_{\min}(\tilde{\mathcal{K}} < 0)} \right|. \tag{23}$$

According to the definition, $\chi_E^{ij} > 0$ ($\chi_{\mathcal{R}} > 0$) indicates the nonreciprocal bipartite (tripartite) entanglement, while $\chi_E^{ij} = 1$ ($\chi_{\mathcal{R}} = 1$) represents ideal nonreciprocity.

In order to more clearly see the dependence of the nonreciprocity of entanglements on the individual parameters, Fig. 4 plots the chiral factors versus Δ_m, $|\tilde{\mathcal{K}}|$, and T, respectively. From Fig. 4(a), it is evident that the chiral factors of all entanglements are responsive to Δ_m, which can be adjusted from 0 to 1 by modifying the detuning. Figure 4(b) illustrates that the nonreciprocal entanglements vanish when the magnon Kerr effect is absent, and appear when it is present. Even when the MPA strength is weak, tripartite entanglement can achieve relatively strong nonreciprocity. As the MPA strength increases gradually, the NVE-NVE entanglement first attains the ideal nonreciprocity, followed by the optimization of nonreciprocity of the magnon-NVE bipartite and tripartite entanglements. Although all bipartite and tripartite entanglements weaken with increasing temperature, the sensitivity of entanglements to temperature varies depending on the case of $\tilde{\mathcal{K}} < 0$ or $\tilde{\mathcal{K}} > 0$, leading to different responses of the chirality factor to temperature. As observed from the Fig. 4(c), the chiral factor of tripartite entanglement remains highly robust with respect to temperature, while that of bipartite entanglements only approaches the ideal value at high temperatures. In summary, we find that the nonreciprocity

of entanglement can be switched off and on by tuning the magnon detuning or the MPA strength, and temperature can also be a promising way to design nonreciprocity.

Finally, we discuss the validity of our model and provide a scheme for detecting and verifying the generated entanglements. Note that the above results are valid only in the low-excitation limit, i.e., $\langle m^\dagger m\rangle \ll 2S$ and $\langle b_l^\dagger b_l\rangle \ll N$. For a 10-μm-diameter YIG sphere, the number of spins $S \simeq 5.52\times 10^{12}$ and the Kerr nonlinear coefficient $\mathcal{K} \simeq 10^{-4}$ Hz [89–92]. Under the optimal parameters in Fig. 2, we obtain $\langle m^\dagger m\rangle \simeq 10^9 \ll 2S \simeq 1.1\times 10^{12}$ and $\langle b_l^\dagger b_l\rangle \simeq 10^{11} \ll N \simeq 10^{12}$, which well satisfy the low-excitation limit. In addition, the states of NVE and magnon can be read out by coupling them to the additional cavities via beam-splitter-like interaction. The generated entanglements can be verified by measuring the corresponding CMs via homodyning the outputs of the probe fields [107,108].

IV. CONCLUSION

In conclusion, we suggest a scheme to realize the nonreciprocal entanglement of magnons and NVEs based on the magnon Kerr effect. The indirect interaction between two separated NVEs and a YIG sphere is established by a common TLR acting as a quantum bus. Interestingly, the Kerr nonlinearity, originated from the driven magnon, leads to the generation of nonreciprocal bipartite and tripartite entanglements. In essence, it is the very MPAs that prepare the magnon mode into a squeezed state and then the nonclassical state is transferred to the NVE modes by the beam-splitter interaction. Simultaneously, the MFS, whose sign depends on the direction of the bias magnetic field, induces nonreciprocity in the hybrid system. In this way, nonreciprocal bipartite, even tripartite, entanglements can be established and controlled flexibly by the system parameters. Although our analysis is based on an all-solid-state system consisting of a single magnon and two NVEs, this scheme can be extended to generate multibody nonreciprocal entanglement on a larger scale. Therefore, our works may provide a valuable direction for the design of on-chip chiral quantum devices.

ACKNOWLEDGMENTS

This work is supported by the National Natural Science Foundation of China (Grants No. 12375011 and No. 12304392) and the National "111 Research Center" Microelectronics Circuits.

APPENDIX A: HAMILTONIAN OF THE YIG SPHERE

As shown in Fig. 1, the YIG sphere is saturated magnetized by a uniform magnetic field $\mathbf{B}_0 = B_0\mathbf{e}_z$, where $\mathbf{e}_x$, $\mathbf{e}_y$, and $\mathbf{e}_z$ are the unit vectors along three orthogonal directions. For the magnetized YIG sphere, the internal magnetic field $\mathbf{H}_{\rm in}$ within the YIG sphere is denoted as

$$\mathbf{H}_{\rm in} = \mathbf{H}_{\rm ex} + \mathbf{H}_{\rm de} + \mathbf{H}_{\rm an}, \tag{A1}$$

where the exchange field $\mathbf{H}_{\rm ex}$ arises from the exchange interaction, the demagnetization field $\mathbf{H}_{\rm de}$ emerges from the magnetic dipole-dipole interaction, and the anisotropic field $\mathbf{H}_{\rm an}$ is induced by the magnetocrystalline anisotropy of the YIG sphere [92,93]. When Zeeman energy is included, the Hamiltonian of the YIG sphere reads (with $\hbar = 1$)

$$H_m = \int_{V_m} \mathbf{M}\cdot\mathbf{B}_0\, d\tau + \int_{V_m} \mathbf{M}\cdot\mathbf{H}_{\rm in}\, d\tau, \tag{A2}$$

where $\mathbf{M} = (M_x, M_y, M_z)$ is the magnetization of the YIG sphere.

In the uniformly magnetized YIG sphere characterized by uniform magnetization $\mathbf{M}$, the exchange field, also known as the molecular field in Weiss theory, is represented as $\mathbf{H}_{\rm ex} = -\Lambda\mathbf{M}$, where Λ denotes the molecular field constant. The induced demagnetizing field is $\mathbf{H}_{\rm de} = -\mathbf{M}/3$ for a YIG sphere. However, the anisotropic field $\mathbf{H}_{\rm an}$ depends on the crystallographic axis of the YIG aligned with the externally applied static field. When the crystallographic axis [100] is aligned along $\mathbf{B}_0$, the anisotropic field can be written as

$$\mathbf{H}_{\rm an} = -\frac{2K_{\rm an}M_z}{M^2}\mathbf{e}_z, \tag{A3}$$

where we only consider the dominant first-order anisotropy constant $K_{\rm an}$ (> 0). Then, the Hamiltonian (A2) of the YIG sphere takes the form

$$H_m = -B_0 M_z V_m + \frac{\mu_0 K_{\rm an} V_m}{M^2} M_z^2, \tag{A4}$$

where the constant term $(1+3\Lambda)\mu_0 V_m/6$, which includes the demagnetization energy and the exchange energy, has been ignored.

The YIG sphere can act as a macrospin $\mathbf{S} = \mathbf{M}V_m/\gamma_0 \equiv (S_x, S_y, S_z)$, where $\gamma_0 = g\mu_B/\hbar$ is the gyromagnetic ratio, with g being the g factor and μ_B being the Bohr magneton. With the macrospin operator introduced, the Hamiltonian H_m reads

$$H_m = -\gamma_0 B_0 S_z + D_x S_x^2 + D_y S_y^2 + D_z S_z^2, \tag{A5}$$

where the nonlinear coefficients are

$$D_x = D_y = 0, \quad D_z = \frac{\mu_0 K_{\rm an}\gamma_0^2}{M^2 V_m}. \tag{A6}$$

However, when the crystalline axis [110] aligns with the bias magnetic field, the exchange field and the demagnetization field remain unchanged, while the anisotropic field

becomes

$$\mathbf{H}_{\mathrm{an}} = -\frac{3K_{\mathrm{an}}M_x}{M^2}\mathbf{e}_x - \frac{9K_{\mathrm{an}}M_y}{4M^2}\mathbf{e}_y - \frac{K_{\mathrm{an}}M_z}{M^2}\mathbf{e}_z. \tag{A7}$$

Using the same approach, we can express the Hamiltonian H_m in a similar form, but with the nonlinear coefficients becoming

$$D_x = \frac{3\mu_0 K_{\mathrm{an}}\gamma_0^2}{2M^2V_m}, \quad D_y = \frac{9\mu_0 K_{\mathrm{an}}\gamma_0^2}{8M^2V_m}, \quad D_z = \frac{\mu_0 K_{\mathrm{an}}\gamma_0^2}{2M^2V_m}. \tag{A8}$$

APPENDIX B: SYSTEM STABILITY ANALYSIS

In general, when investigating the properties of entanglement, it is imperative to focus on the stability of the system. Here, the stability of the system can be determined by analyzing the eigenvalues of the coefficient matrix A. Initially, we formulate the eigenequation corresponding to Eq. (15),

$$A\mu = \lambda\mu, \tag{B1}$$

and subsequently compute the eigenvalues in the usual way, by setting $|A - \lambda I| = 0$. This yields the characteristic equation [74]

$$a_0\lambda^6 + a_1\lambda^5 + a_2\lambda^4 + a_3\lambda^3 + a_4\lambda^2 + a_5\lambda + a_6 = 0. \tag{B2}$$

The corresponding coefficients are as follows:

$$\begin{aligned}
a_0 &= 1,\\
a_1 &= 2\gamma + \kappa_m,\\
a_2 &= 4g_1^2 + 2g_2^2 - 4\widetilde{\mathcal{K}}^2 + \frac{3}{2}\gamma^2 + 2\gamma\kappa_m + \frac{1}{4}\kappa_m^2 + \widetilde{\Delta}_m^2 + 2\Delta_n^2,\\
a_3 &= 6g_1^2\gamma + 2g_2^2\gamma - 8\widetilde{\mathcal{K}}^2\gamma + \frac{1}{2}\gamma^3 + 2g_1^2\kappa_m + 2g_2^2\kappa_m + \frac{3}{2}\gamma^2\kappa_m + \frac{1}{2}\gamma\kappa_m^2 + 2\gamma\widetilde{\Delta}_m^2 + 2\gamma\Delta_n^2,\\
a_4 &= 4g_1^4 + 4g_1^2g_2^2 + g_2^4 - 8g_2^2\widetilde{\mathcal{K}}^2 + 3g_1^2\gamma^2 + \frac{1}{2}g_2^2\gamma^2 - 6\widetilde{\mathcal{K}}^2\gamma^2\\
&\quad + \frac{1}{16}\gamma^4 + 3g_1^2\gamma\kappa_m + 2g_2^2\gamma\kappa_m + \frac{1}{2}\gamma^3\kappa_m + \frac{1}{2}g_2^2\kappa_m^2\\
&\quad + \frac{3}{8}\gamma^2\kappa_m^2 - 4g_1^2g_2\widetilde{\Delta}_m + 2g_2^2\widetilde{\Delta}_m^2 + \frac{3}{2}\gamma^2\widetilde{\Delta}_m^2 - 8g_1^2g_2\Delta_n\\
&\quad - 4g_1^2\widetilde{\Delta}_m\Delta_n + 4g_1^2\Delta_n^2 - 2g_2^2\Delta_n^2 - 8\widetilde{\mathcal{K}}^2\Delta_n^2 + \frac{1}{2}\gamma^2\Delta_n^2\\
&\quad + 2\gamma\kappa_m\Delta_n^2 + \frac{1}{2}\kappa_m^2\Delta_n^2 + 2\widetilde{\Delta}_m^2\Delta_n^2 + \Delta_n^4,\\
a_5 &= 4g_1^4\gamma + 2g_1^2g_2^2\gamma - 8g_2^2\widetilde{\mathcal{K}}^2\gamma + \frac{1}{2}g_1^2\gamma^3 - 2\widetilde{\mathcal{K}}^2\gamma^3 + 2g_1^2g_2^2\kappa_m\\
&\quad + g_2^4\kappa_m + \frac{3}{2}g_1^2\gamma^2\kappa_m + \frac{1}{2}g_2^2\gamma^2\kappa_m + \frac{1}{16}\gamma^4\kappa_m + \frac{1}{2}g_2^2\gamma\kappa_m^2\\
&\quad + \frac{1}{8}\gamma^3\kappa_m^2 - 4g_1^2g_2\gamma\widetilde{\Delta}_m + 2g_2^2\gamma\widetilde{\Delta}_m^2 + \frac{1}{2}\gamma^3\widetilde{\Delta}_m^2 - 4g_1^2g_2\gamma\Delta_n\\
&\quad - 4g_1^2g_2\kappa_m\Delta_n - 4g_1^2\gamma\widetilde{\Delta}_m\Delta_n + 2g_1^2\gamma\Delta_n^2 - 8\widetilde{\mathcal{K}}^2\gamma\Delta_n^2\\
&\quad + 2g_1^2\kappa_m\Delta_n^2 - 2g_2^2\kappa_m\Delta_n^2 + \frac{1}{2}\gamma^2\kappa_m\Delta_n^2 + \frac{1}{2}\gamma\kappa_m^2\Delta_n^2\\
&\quad + 2\gamma\widetilde{\Delta}_m^2\Delta_n^2 + \kappa_m\Delta_n^4,\\
a_6 &= 4g_1^4g_2^2 - 4g_2^4\widetilde{\mathcal{K}}^2 + g_1^4\gamma^2 - 2g_2^2\widetilde{\mathcal{K}}^2\gamma^2 - \frac{1}{4}\widetilde{\mathcal{K}}^2\gamma^4 + g_1^2g_2^2\gamma\kappa_m\\
&\quad + \frac{1}{4}g_1^2\gamma^3\kappa_m + \frac{1}{4}g_2^4\kappa_m^2 + \frac{1}{8}g_2^2\gamma^2\kappa_m^2 + \frac{1}{64}\gamma^4\kappa_m^2 - 4g_1^2g_2^3\widetilde{\Delta}_m
\end{aligned}$$

$$
\begin{aligned}
&- g_1^2 g_2 \gamma^2 \widetilde{\Delta}_m + g_2^4 \widetilde{\Delta}_m^2 + \frac{1}{2} g_2^2 \gamma^2 \widetilde{\Delta}_m^2 + \frac{1}{16} \gamma^4 \widetilde{\Delta}_m^2 - 8 g_1^4 g_2 \Delta_n \\
&- 2 g_1^2 g_2 \gamma \kappa_m \Delta_n + 4 g_1^2 g_2^2 \widetilde{\Delta}_m \Delta_n - g_1^2 \gamma^2 \widetilde{\Delta}_m \Delta_n + 4 g_1^4 \Delta_n^2 \\
&+ 8 g_2^2 \widetilde{\mathcal{K}}^2 \Delta_n^2 - 2 \widetilde{\mathcal{K}}^2 \gamma^2 \Delta_n^2 + g_1^2 \gamma \kappa_m \Delta_n^2 - \frac{1}{2} g_2^2 \kappa_m^2 \Delta_n^2 \\
&+ \frac{1}{8} \gamma^2 \kappa_m^2 \Delta_n^2 + 4 g_1^2 g_2 \widetilde{\Delta}_m \Delta_n^2 - 2 g_2^2 \widetilde{\Delta}_m^2 \Delta_n^2 + \frac{1}{2} \gamma^2 \widetilde{\Delta}_m^2 \Delta_n^2 \\
&- 4 g_1^2 \widetilde{\Delta}_m \Delta_n^3 - 4 \widetilde{\mathcal{K}}^2 \Delta_n^4 + \frac{1}{4} \kappa_m^2 \Delta_n^4 + \widetilde{\Delta}_m^2 \Delta_n^4 .
\end{aligned} \tag{B3}
$$

Since we only wish to know the character of the eigenvalues, there is no necessity to solve Eq. (B2) for λ. According to the Routh-Hurwitz criterion [97], all eigenvalues are negative or have negative real parts (i.e., the system is stable), if the following condition is met:

$$
T_n = \begin{vmatrix}
M_{11} & M_{12} & M_{13} & \cdots & M_{1n} \\
M_{21} & M_{22} & M_{23} & \cdots & M_{2n} \\
M_{31} & M_{32} & M_{33} & \cdots & M_{3n} \\
\vdots & \vdots & \vdots & & \vdots \\
M_{n1} & M_{n2} & M_{n3} & \cdots & M_{nn}
\end{vmatrix} > 0, \tag{B4}
$$

where T_n is the determinant of the $n \times n$ matrix M_{ij} for $n =$ 1–6. The matrix M_{ij} is formed using this rule: if $2i - j <$ 0 or $2i - j > 6$, then $M_{ij} = 0$; otherwise, $M_{ij} = a_{2i-j}$. To ensure that the obtained entanglements are in the stability region, we numerically plot the functions T_n, highlighting the unstable regions with shading in Figs. 2 and 3.

[1] A. Einstein, B. Podolsky, and N. Rosen, Can quantum-mechanical description of physical reality be considered complete, Phys. Rev. **47**, 777 (1935).

[2] R. Horodecki, P. Horodecki, M. Horodecki, and K. Horodecki, Quantum entanglement, Rev. Mod. Phys. **81**, 865 (2009).

[3] E. Chitambar and G. Gour, Quantum resource theories, Rev. Mod. Phys. **91**, 025001 (2019).

[4] T. D. Ladd, F. Jelezko, R. Laflamme, Y. Nakamura, C. Monroe, and J. L. Orien, Quantum computers, Nature (London) **464**, 45 (2010).

[5] A. J. Leggett, Macroscopic quantum systems and the quantum theory of measurement, Prog. Theor. Phys. **69**, 80 (1980).

[6] A. J. Leggett, Testing the limits of quantum mechanics: Motivation, state of play, prospects, J. Phys.: Condens. Matter **14**, R415 (2002).

[7] Y. Chen, Macroscopic quantum mechanics: Theory and experimental concepts of optomechanics, J. Phys. B **46**, 104001 (2013).

[8] F. Fröwis, P. Sekatski, W. Dür, N. Gisin, and N. Sangouard, Macroscopic quantum states: Measures fragility, and implementations, Rev. Mod. Phys. **90**, 025004 (2018).

[9] A. Bassi, K. Lochan, S. Satin, T. P. Singh, and H. Ulbricht, Models of wave-function collapse underlying theories, and experimental tests, Rev. Mod. Phys. **85**, 471 (2013).

[10] M. J. Weaver, D. Newsom, F. Luna, W. Löffler, and D. Bouwmeester, Phonon interferometry for measuring quantum decoherence, Phys. Rev. A **97**, 063832 (2018).

[11] C. Marletto and V. Vedral, Gravitationally induced entanglement between two massive particles is sufficient evidence of quantum effects in gravity, Phys. Rev. Lett. **119**, 240402 (2017).

[12] D. Lachance-Quirion, Y. Tabuchi, A. Gloppe, K. Usami, and Y. Nakamura, Hybrid quantum systems based on magnonics, Appl. Phys. Express **12**, 070101 (2019).

[13] Z. Zhang, M. O. Scully, and G. S. Agarwal, Quantum entanglement between two magnon modes via Kerr nonlinearity driven far from equilibrium, Phys. Rev. Res. **1**, 023021 (2019).

[14] J. Li and S.-Y. Zhu, Entangling two magnon modes via magnetostrictive interaction, New J. Phys. **21**, 085001 (2019).

[15] D. Y. Kong, X. M. Hu, L. Hu, and J. Xu, Magnon-atom interaction via dispersive cavities: Magnon entanglement, Phys. Rev. B **103**, 224416 (2021).

[16] H. T. Tan and J. Li, Einstein-Podolsky-Rosen entanglement and asymmetric steering between distant macroscopic mechanical and magnonic systems, Phys. Rev. Res. **3**, 013192 (2021).

[17] J. Li, S.-Y. Zhu, and G. S. Agarwal, Magnon-photon-phonon entanglement in cavity magnomechanics, Phys. Rev. Lett. **121**, 203601 (2018).

[18] F. Wang, C. D. Gou, J. Xu, and C. Gong, Hybrid magnon-atom entanglement and magnon blockade via quantum interference, Phys. Rev. A **106**, 013705 (2022).

[19] Z.-Y. Fan, H. Qian, X. Zuo, and J. Li, Entangling ferrimagnetic magnons with an atomic ensemble via optomagnomechanics, Phys. Rev. A **108**, 023501 (2023).

[20] Y. Wu, J.-H. Liu, Y.-F. Yu, Z.-M. Zhang, and J.-D. Wang, Entangling a magnon and an atomic ensemble mediated by an optical cavity, Phys. Rev. Appl. **20**, 04043 (2023).

[21] M. W. Doherty, N. B. Manson, P. Delaney, F. Jelezko, J. Wrachtrup, and L. C. L. Hollenberg, The nitrogen-vacancy colour centre in diamond, Phys. Rep. **528**, 1 (2013).

[22] P. Neumann, R. Kolesov, B. Naydenov, J. Beck, F. Rempp, M. Steiner, V. Jacques, G. Balasubramanian, M. L. Markham, and D. J. Twitchen, Quantum register based

on coupled electron spins in a room-temperature solid, Nat. Phys. **6**, 249 (2010).
[23] G. Balasubramanian, P. Neumann, D. Twitchen, M. Markham, R. Kolesov, N. Mizuochi, J. Isoya, J. Achard, J. Beck, J. Tissler, V. Jacques, P. R. Hemmer, F. Jelezko, and J. Wrachtrup, Ultralong spin coherence time in isotopically engineered diamond, Nat. Mater. **8**, 383 (2009).
[24] N. Bar-Gill, L. M. Pham, A. Jarmola, D. Budker, and R. L. Walsworth, Solid-state electronic spin coherence time approaching one second, Nat. Commun. **4**, 1743 (2013).
[25] P. C. Maurer, G. Kucsko, C. Latta, L. Jiang, N. Y. Yao, S. D. Bennett, F. Pastawski, D. Hunger, N. Chisholm, M. Markham, D. J. Twitchen, J. I. Cirac, and M. D. Lukin, Room-temperature quantum bit memory exceeding one second, Science **336**, 1283 (2012).
[26] Y. Kubo, F. R. Ong, P. Bertet, D. Vion, V. Jacques, D. Zheng, A. Dréau, J.-F. Roch, A. Auffeves, F. Jelezko, J. Wrachtrup, M. F. Barthe, P. Bergonzo, and D. Esteve, Strong coupling of a spin ensemble to a superconducting resonator, Phys. Rev. Lett. **105**, 140502 (2010).
[27] D. Marcos, M. Wubs, J. M. Taylor, R. Aguado, M. D. Lukin, and A. S. Sørensen, Coupling nitrogen-vacancy centers in diamond to superconducting flux qubits, Phys. Rev. Lett. **105**, 210501 (2010).
[28] G. D. Fuchs, V. V. Dobrovitski, R. Hanson, A. Batra, C. D. Weis, T. Schenkel, and D. D. Awschalom, Single-shot readout of multiple nuclear spin qubits in diamond under ambient conditions, Phys. Rev. Lett. **101**, 117601 (2008).
[29] G. D. Fuchs, V. V. Dobrovitski, D. M. Toyli, F. J. Heremans, and D. D. Awschalom, Gigahertz dynamics of a strongly driven single quantum spin, Science **326**, 1520 (2009).
[30] T. Neuman, D. S. Wang, and P. Narang, Nanomagnonic cavities for strong spin-magnon coupling and magnon-mediated spin-spin interactions, Phys. Rev. Lett. **125**, 247702 (2020).
[31] D. R. Candido, G. D. Fuchs, E. Johnston-Halperin, and M. E. Flatté, Predicted strong coupling of solid-state spins via a single magnon mode, Mat. Quantum Technol. **1**, 011001 (2020).
[32] M. Fukami, D. R. Candido, D. D. Awschalom, and M. E. Flatté, Opportunities for long-range magnon-mediated entanglement of spin qubits via on- and off-resonant coupling, PRX Quantum **2**, 040314 (2021).
[33] X.-L. Hei, P.-B. Li, X.-F. Pan, and F. Nori, Enhanced tripartite interactions in spin-magnon-mechanical hybrid systems, Phys. Rev. Lett. **130**, 073602 (2023).
[34] W. Xiong, M. Wang, G.-Q. Zhang, and J. Chen, Optomechanical-interface-induced strong spin-magnon coupling, Phys. Rev. A **107**, 033516 (2023).
[35] W. L. Yang, Y. Hu, Z. Q. Yin, Z. J. Deng, and M. Feng, Entanglement of nitrogen-vacancy-center ensembles using transmission line resonators and a superconducting phase qubit, Phys. Rev. A **83**, 022302 (2011).
[36] M.-J. Tao, M. Hua, Q. Ai, and F.-G. Deng, Quantum-information processing on nitrogen-vacancy ensembles with the local resonance assisted by circuit QED, Phys. Rev. A **91**, 062325 (2015).
[37] W.-J. Su, Z.-B. Yang, and Z.-R. Zhong, Arbitrary control of entanglement between two nitrogen-vacancy-center ensembles coupling to a superconducting-circuit qubit, Phys. Rev. A **97**, 012329 (2018).
[38] S.-L. Ma, X.-K. Li, J.-K Xie, and F.-L. Li, Two-mode squeezed states of two separated nitrogen-vacancy-center ensembles coupled via dissipative photons of superconducting resonators, Phys. Rev. A **99**, 012325 (2019).
[39] Q. Z. Hou, C. J. Yang, C. Y. Chen, J. H. An, W. L. Yang, and M. Feng, Preservation of quantum correlation between nitrogen-vacancy-center ensembles by squeezed-reservoir engineering, Phys. Rev. A **100**, 032302 (2019).
[40] Y.-H. Ma, Q.-Z. Ding, and E. Wu, Entanglement of two nitrogen-vacancy ensembles via a nanotube, Phys. Rev. A **101**, 022311 (2020).
[41] A. Pradana and L. Y. Chew, Entanglement of nitrogen-vacancy-center ensembles with initial squeezing, Phys. Rev. A **104**, 022435 (2021).
[42] Y. Shoji and T. Mizumoto, Magneto-optical nonreciprocal devices in silicon photonics, Sci. Technol. Adv. Mater. **15**, 014602 (2014).
[43] D.-W. Wang, H.-T. Zhou, M.-J. Guo, J.-X. Zhang, J. Evers, and S.-Y. Zhu, Optical diode made from a moving photonic crystal, Phys. Rev. Lett. **110**, 093901 (2013).
[44] Y. Yang, C. Peng, D. Zhu, H. Buljan, J. D. Joannopoulos, B. Zhen, and M. Soljačić, Synthesis and observation of non-Abelian gauge fields in real space, Science **365**, 1021 (2019).
[45] S. Maayani, R. Dahan, Y. Kligerman, E. Moses, A. U. Hassan, H. Jing, F. Nori, D. N. Christodoulides, and T. Carmon, Flying couplers above spinning resonators generate irreversible refraction, Nature (London) **558**, 569 (2018).
[46] D. L. Sounas and A. Alù, Non-reciprocal photonics based on time modulation, Nat. Photonics **11**, 774 (2017).
[47] B. Peng, S. K. Özdemir, F. Lei, F. Monifi, M. Gianfreda, G. L. Long, S. Fan, F. Nori, C. M. Bender, and L. Yang, Parity-time-symmetric whispering-gallery microcavities, Nat. Phys. **10**, 394 (2014).
[48] Q. Zhong, S. Nelson, Ş. K. Özdemir, and R. El-Ganainy, Controlling directional absorption with chiral exceptional surfaces, Opt. Lett. **44**, 5242 (2019).
[49] C.-H. Dong, Z. Shen, C.-L. Zou, Y.-L. Zhang, W. Fu, and G.-C. Guo, Brillouin-scattering-induced transparency and non-reciprocal light storage, Nat. Commun. **6**, 6193 (2015).
[50] J. Kim, M. C. Kuzyk, K. Han, H. Wang, and G. Bahl, Non-reciprocal Brillouin scattering induced transparency, Nat. Phys. **11**, 275 (2015).
[51] X.-W. Xu, Y. Li, B. Li, H. Jing, and A.-X. Chen, Nonreciprocity via nonlinearity and synthetic magnetism, Phys. Rev. Appl. **13**, 044070 (2020).
[52] S. Manipatruni, J. T. Robinson, and M. Lipson, Optical nonreciprocity in optomechanical structures, Phys. Rev. Lett. **102**, 213903 (2009).
[53] Z. Shen, Y.-L. Zhang, Y. Chen, C.-L. Zou, Y.-F. Xiao, X.-B. Zou, F.-W. Sun, G.-C. Guo, and C.-H. Dong, Experimental realization of optomechanically induced non-reciprocity, Nat. Photonics **10**, 657 (2016).
[54] N. R. Bernier, L. D. Toth, A. Koottandavida, M. A. Ioannou, D. Malz, A. Nunnenkamp, A. K. Feofanov, and T. J. Kippenberg, Nonreciprocal reconfigurable

microwave optomechanical circuit, Nat. Commun. **8**, 604 (2017).
[55] K. Fang, J. Luo, A. Metelmann, M. H. Matheny, F. Marquardt, A. A. Clerk, and O. Painter, Generalized non-reciprocity in an optomechanical circuit via synthetic magnetism and reservoir engineering, Nat. Phys. **13**, 465 (2017).
[56] H. Ramezani, P. K. Jha, Y. Wang, and X. Zhang, Non-reciprocal localization of photons, Phys. Rev. Lett. **120**, 043901 (2018).
[57] S. Zhang, Y. Hu, G. Lin, Y. Niu, K. Xia, J. Gong, and S. Gong, Thermal-motion-induced non-reciprocal quantum optical system, Nat. Photonics **12**, 744 (2018).
[58] Y. Jiang, S. Maayani, T. Carmon, Franco Nori, and H. Jing, Nonreciprocal phonon laser, Phys. Rev. Appl. **10**, 064037 (2018).
[59] Y. Xu, J.-Y. Liu, W. Liu, and Y.-F. Xiao, Nonreciprocal phonon laser in a spinning microwave magnomechanical system, Phys. Rev. A **103**, 053501 (2021).
[60] H. Zhang, R. Huang, S.-D. Zhang, Y. Li, C.-W. Qiu, F. Nori, and H. Jing, Breaking anti-*PT* symmetry by spinning a resonator, Nano Lett. **20**, 7594 (2020).
[61] S. Jiang, Z. Xiao, W. Li, T. Chen, J. Li, A. Huang, and H. Zhang, Enhanced nanoparticle sensing by mode intensity in a non-reciprocally coupled microcavity, J. Appl. Phys. **131**, 103106 (2022).
[62] I. M. Mirza, W. Ge, and H. Jing, Optical nonreciprocity and slow light in coupled spinning optomechanical resonators, Opt. Express **27**, 25515 (2019).
[63] M. Peng, H. Zhang, Q. Zhang, T. X. Lu, I. M. Mirza, and H. Jing, Nonreciprocal slow or fast light in anti-$\mathscr{P}\mathscr{T}$-symmetric optomechanics, Phys. Rev. A **107**, 033507 (2023).
[64] B. Li, Ş. K. Özdemir, X.-W. Xu, L. Zhang, L.-M. Kuang, and H. Jing, Nonreciprocal optical solitons in a spinning Kerr resonator, Phys. Rev. A **103**, 053522 (2021).
[65] R. Huang, A. Miranowicz, J.-Q. Liao, F. Nori, and H. Jing, Nonreciprocal Photon Blockade, Phys. Rev. Lett. **121**, 153601 (2018).
[66] X.-Y. Yao, H. Ali, F.-L. Li, and P.-B. Li, Nonreciprocal phonon blockade in a spinning acoustic ring cavity coupled to a two-level system, Phys. Rev. A **17**, 054004 (2022).
[67] Y. Wang, W. Xiong, Z. Xu, G.-Q. Zhang, and J.-Q. You, Dissipation-induced nonreciprocal magnon blockade in a magnon-based hybrid system, Sci. China Phys. Mech. Astron. **65**, 260314 (2022).
[68] W. Zhang, T. Wang, S. Liu, S. Zhang, and H.-F. Wang, Nonreciprocal photon blockade in a spinning resonator coupled to two two-level atoms, Sci. China Phys. Mech. Astron. **66**, 240313 (2023).
[69] C. D. Gou and X. M. Hu, Simultaneous nonreciprocal photon blockade in two coupled spinning resonators via Sagnac-Fizeau shift and parametric amplification, Phys. Rev. A **108**, 043723 (2023).
[70] K. Xia, G. Lu, G. Lin, Y. Cheng, Y. Niu, S. Gong, and J. Twamley, Reversible nonmagnetic single-photon isolation using unbalanced quantum coupling, Phys. Rev. A **90**, 043802 (2014).
[71] K. Xia, F. Nori, and M. Xiao, Cavity-free optical isolators and circulators using a chiral cross-kerr nonlinearity, Phys. Rev. Lett. **121**, 203602 (2018).
[72] Y.-F. Jiao, S.-D. Zhang, Y.-L. Zhang, A. Miranowicz, L.-M. Kuang, and H. Jing, Nonreciprocal optomechanical entanglement against backscattering losses, Phys. Rev. Lett. **125**, 143605 (2020).
[73] Y.-F. Jiao, J.-X. Liu, Y. Li, R. Yang, L.-M. Kuang, and H. Jing, Nonreciprocal enhancement of remote entanglement between nonidentical mechanical oscillators, Phys. Rev. Appl. **18**, 064008 (2022).
[74] J.-X. Liu, Y.-F. Jiao, Y. Li, X.-W. Xu, Q.-Y. He, and H. Jing, Phase-controlled asymmetric optomechanical entanglement against optical backscattering, Sci. China Phys. Mech. Astron. **66**, 230312 (2023).
[75] Y.-L. Ren, Nonreciprocal optical-microwave entanglement in a spinning magnetic resonator, Opt. Lett. **44**, 1125 (2022).
[76] J. J. Chen, X.-G. Fan, W. Xiong, D. Wang, and L. Ye, Nonreciprocal entanglement in cavity-magnon optomechanics, Phys. Rev. B **108**, 024105 (2023).
[77] Q. J. Zheng, W. X. Zhong, G. L. Cheng, and A. X. Chen, Nonreciprocal tripartite entanglement based on magnon Kerr effect in a spinning microwave resonator, Opt. Commun. **546**, 129796 (2023).
[78] S.-Y. Guan, H.-F. Wang, and X. Yi, Cooperative-effect-induced one-way steering in open cavity magnonics, npj Quantum Inf. **8**, 102 (2022).
[79] W. Zhong, Q. Zheng, G. Cheng, and A. Chen, Nonreciprocal genuine steering of three macroscopic samples in a spinning microwave magnonical system, Appl. Phys. Lett. **123**, 134003 (2023).
[80] A. Graf, S. D. Rogers, J. Staffa, U. A. Javid, D. H. Griffith, and Q. Lin, Nonreciprocity in photon pair correlations of classically reciprocal systems, Phys. Rev. Lett. **128**, 213605 (2022).
[81] P. Yang, M. Li, X. Han, H. He, G. Li, C.-L. Zou, P. Zhang, Y. Qian, and T. Zhang, Non-reciprocal cavity polariton with atoms strongly coupled to optical cavity, Laser & Photonics Rev. **17**, 2200574 (2023).
[82] P. Lodahl, S. Mahmoodian, S. Stobbe, A. Rauschenbeutel, P. Schneeweiss, J. Volz, H. Pichler, and P. Zoller, Chiral quantum optics, Nature (London) **541**, 473 (2017).
[83] T. Holstein and H. Primakoff, Field dependence of the intrinsic domain magnetization of a ferromagnet, Phys. Rev. **58**, 1098 (1940).
[84] Y. Tabuchi, S. Ishino, A. Noguchi, T. Ishikawa, R. Yamazaki, K. Usami, and Y. Nakamura, Quantum magnonics: The magnon meets the superconducting qubit, C. R. Phys. **117**, 729 (2016).
[85] Y. Tabuchi, S. Ishino, A. Noguchi, T. Ishikawa, R. Yamazaki, K. Usami, and Y. Nakamura, Coherent coupling between a ferromagnetic magnon and a superconducting qubit, Science **349**, 405 (2015).
[86] D. Lachance-Quirion, Y. Tabuchi, S. Ishino, A. Noguchi, T. Ishikawa, R. Yamazaki, and Y. Nakamura, Resolving quanta of collective spin excitations in a millimeter-sized ferromagnet, Sci. Adv. **3**, e1603150 (2017).

[87] W. Huang, Y. Wu, and X.-Y. Lü, Superradiant phase transition induced by the indirect Rabi interaction, Phys. Rev. A **107**, 033702 (2023).
[88] A. V. Chumak, V. I. Vasyuchka, A. A. Serga, and B. Hillebrands, Magnon spintronics, Nat. Phys. **11**, 453 (2015).
[89] Y. P. Wang, G. Q. Zhang, D. Zhang, T. F. Li, C. M. Hu, and J. Q. You, Bistability of cavity magnon polaritons, Phys. Rev. Lett. **120**, 057202 (2018).
[90] R. C. Shen, Y. P. Wang, J. Li, S. Y. Zhu, G. S. Agarwal, and J. Q. You, Long-time memory and ternary logic gate using a multistable cavity magnonic system, Phys. Rev. Lett. **127**, 183202 (2021).
[91] L. Bai, Michael Harder, Paul Hyde, Z. Zhang, C.-M. Hu, Y. P. Chen, and John Q. Xiao, Cavity mediated manipulation of distant spin currents using a cavity-magnon-polariton, Phys. Rev. Lett. **118**, 217201 (2017).
[92] Y.-P. Wang, G.-Q. Zhang, D. Zhang, X.-Q. Luo, W. Xiong, S.-P. Wang, T.-F. Li, C.-M. Hu, and J. Q. You, Magnon Kerr effect in a strongly coupled cavity-magnon system, Phys. Rev. B **94**, 224410 (2016).
[93] G.-Q. Zhang, Y.-P. Wang, and J. Q. You, Theory of the magnon Kerr effect in cavity magnonics, Sci. China Phys. Mech. Astron. **62**, 987511 (2019).
[94] M. O. Scully and M. S. Zubairy, *Quantum Optics* (Cambridge University Press, Cambridge, 1997).
[95] D. F. Walls and G. J. Milburn, *Quantum Optics* (Springer, Berlin, 1994).
[96] C. W. Gardiner and P. Zoller, *Quantum Noise* (Springer, Berlin, 2000), 2nd ed.
[97] E. X. DeJesus and C. Kaufman, Routh-Hurwitz criterion in the examination of eigenvalues of a system of nonlinear ordinary differential equations, Phys. Rev. A **35**, 5288 (1987).
[98] D. Vitali, S. Gigan, A. Ferreira, H. R. Bohm, P. Tombesi, A. Guerreiro, V. Vedral, A. Zeilinger, and M. Aspelmeyer, Optomechanical entanglement between a movable mirror and a cavity field, Phys. Rev. Lett. **98**, 030405 (2007).
[99] P. C. Parks and V. Hahn, *Stability Theory* (Prentice Hall, New York, 1993).
[100] G. Vidal and R. F. Werner, Computable measure of entanglement, Phys. Rev. A **65**, 032314 (2002).
[101] M. B. Plenio, Logarithmic negativity: A full entanglement monotone that is not convex, Phys. Rev. Lett. **95**, 090503 (2005).
[102] G. Adesso and F. Illuminati, Entanglement in continuous-variable systems: Recent advances and current perspectives, J. Phys. A: Math. Theor. **40**, 7821 (2007).
[103] V. Coffman, J. Kundu, and W. K. Wootters, Distributed entanglement, Phys. Rev. A **61**, 052306 (2000).
[104] X.-Y. Lü, Y. Wu, J. R. Johansson, H. Jing, J. Zhang, and F. Nori, Squeezed optomechanics with phase-matched amplification and dissipation, Phys. Rev. Lett. **114**, 093602 (2015).
[105] W. Xiong, M. Tian, G.-Q. Zhang, and J. Q. You, Strong long-range spin-spin coupling via a Kerr magnon interface, Phys. Rev. B **105**, 245310 (2022).
[106] Z. Zhang, M. O. Scully, and G. S. Agarwal, Quantum entanglement between two magnon modes via Kerr nonlinearity driven far from equilibrium, Phys. Rev. Res. **1**, 023021 (2019).
[107] T. A. Palomaki, J. D. Teufel, R. W. Simmonds, and K. W. Lehnert, Entangling mechanical motion with microwave fields, Science **342**, 710 (2013).
[108] C. W. Gardiner, Inhibition of atomic phase decays by squeezed light: A direct effect of squeezing, Phys. Rev. Lett. **56**, 1917 (1986).